

Schottky-Barrier-Induced Asymmetry in the Negative-Differential-Resistance Response of Nb/NbO_x/Pt Cross-Point Devices

Shimul Kanti Nath^{1,*}, Sanjoy Kumar Nandi,¹ Assaad El-Helou², Xinjun Liu³, Shuai Li,^{1,4}
Thomas Ratcliff,¹ Peter E. Raad,² and Robert G. Elliman^{1,†}

¹*Department of Electronic Materials Engineering, Research School of Physics, The Australian National University, Canberra ACT 2601, Australia*

²*Department of Mechanical Engineering, Southern Methodist University, Texas, Dallas 75205, USA*

³*Tianjin Key Laboratory of Low Dimensional Materials Physics and Preparation Technology, Faculty of Science, Tianjin University, Tianjin 300354, China*

⁴*Unité Mixte de Physique, CNRS, Thales, Université Paris-Sud, Université Paris-Saclay, Palaiseau 91767, France*



(Received 16 February 2020; accepted 23 April 2020; published 9 June 2020)

The negative-differential-resistance (NDR) response of Nb/NbO_x/Pt cross-point devices is shown to have a polarity dependence due to the effect of the metal-oxide Schottky barriers on the contact resistance. Three distinct responses are observed under opposite polarity testing: bipolar S-type NDR, bipolar snap-back NDR, and combined S-type and snapback NDR, depending on the stoichiometry of the oxide film and device area. *In situ* thermoreflectance imaging is used to show that these NDR responses are associated with strong current localization, thereby justifying the use of a previously developed two-zone, core-shell thermal model of the device. The observed polarity-dependent NDR responses, and their dependence on stoichiometry and area, are then explained by extending this model to include the effect of the polarity-dependent contact resistance. This study provides an improved understanding of the NDR response of metal-oxide-metal structures and informs the engineering of devices for neuromorphic computing and nonvolatile memory applications.

DOI: 10.1103/PhysRevApplied.13.064024

I. INTRODUCTION

Two terminal metal-oxide-metal (MOM) devices using transition metal oxides (TMOs) are of increasing interest for next-generation nonvolatile memory technology and brain-inspired computing [1–3]. Many TMOs exhibit threshold switching or current-controlled negative-differential-resistance (NDR) responses including NbO_x [1,3–6], TaO_x [7–9], VO_x [10,11], TiO_x [12], and NiO_x [13], and MOM devices exploiting these characteristics are of great interest for applications such as self-sustained and chaotic oscillators [2,14], threshold logic devices [15,16], trigger comparators [17], small-signal amplifiers [18,19], and emulators of biological neuronal functionalities [20,21]. Recently, much attention has been given to devices based on NbO_x and VO_x due to their ability to show reliable threshold switching [22] and current-controlled negative differential resistance [1,2,4,23]. Importantly, the functionality of devices is controlled by their specific current-voltage characteristics (e.g., specific NDR mode) [3,14,24], and therefore it is essential to understand the

physical origin of the NDR response and its dependence on material and device parameters.

A reliable NDR response is often observed after an initial electroforming step that creates a filamentary conduction path through the film. This can cause a significant increase in temperature due to local Joule heating [25] and thereby modify the oxide stoichiometry and interfacial Schottky barriers. Changes in the filament due to the generation, drift, and diffusion of oxygen vacancies can also result in competition between resistive and threshold switching, in which case it is necessary to limit the operating current [26] or bias polarity in order to achieve pure threshold switching [27]. Threshold switching then occurs in a small volume between the residual filament and electrode due to the localized current flow in this region [26]. Further details of the electroforming process in NbO_x and its dependence on oxide stoichiometry can be found in our recent study [28].

Studies have shown that NbO_x-based devices can exhibit a range of characteristic NDR modes, including continuous S-type and discontinuous snapback characteristics as well as more complex combinations of these modes [5,24]. The physical origin of S-type NDR is well explained by thermally induced conductivity changes

*shimul.nath@anu.edu.au

†rob.elliman@anu.edu.au

induced by local Joule heating [6,29] and can, in principle, arise from any electrical conduction mechanism that has a superlinear temperature dependence [30]. In contrast, the origin of snapback NDR was initially attributed to the insulator-metal transition (IMT) associated with a Mott-Peierls transition observed in NbO_2 [5]. However, a subsequent study based on finite-element modeling of TaO_x and VO_x devices showed that a similar response could be induced by current localization without recourse to a material-specific phase transition [7]. In an attempt to resolve this issue and explain the diverse range of NDR modes observed in metal-oxide-metal (MOM) devices, we recently developed a core-shell model of NDR [24]. This model is based on the fact that the current distribution in MOM structure is highly localized after electroforming, with the NDR response dominated by the region of highest current density (core) and the surrounding film (shell) acting as a parallel resistance. The threshold-switching response then depends on the relative magnitudes of the maximum negative differential resistance (R_{NDR}) of the core and the shell resistance (R_S). Specifically, S-type NDR is observed for $R_S > R_{\text{NDR}}$ and snapback characteristic is observed for $R_S < R_{\text{NDR}}$, notably, without considering any phase transition.

The parallel resistance (R_S) is determined by the area, thickness and resistivity of the oxide film and the contact resistance created by the metal-oxide interfaces. For devices fabricated with near-stoichiometric oxide films the parallel resistance (R_S) is typically dominated by the film resistivity such that $R_S > R_{\text{NDR}}$ and they exhibit S-type NDR [26,27]. However, for more conductive substoichiometric films the contact resistance is expected to make a significant contribution to the parallel resistance and thereby influence the threshold-switching mode as well as the device stability and reproducibility [24,31,32].

In the present work, we demonstrate that the interface resistance originating from the Schottky barriers at the metal-oxide interfaces can indeed result in distinct NDR modes depending on the operating bias polarity, device area, and oxide conductivity. This is achieved by combining *in situ* thermoreflectance imaging and temperature-dependent electrical testing of NbO_x cross-point devices, and interpreting the results with reference to the above-mentioned core-shell model of NDR.

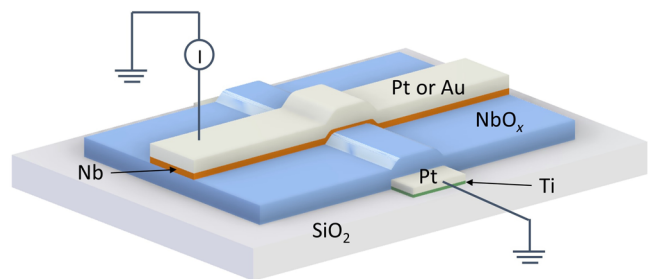


FIG. 1. Three-dimensional schematic of the cross-point device with corresponding material layers.

II. EXPERIMENTAL DETAILS

Cross-point devices with a metal-oxide-metal structure as shown in Fig. 1(a) are fabricated on a thermally oxidized Si (100) wafer with a 300-nm-thick oxide layer using a three-mask photolithography process [25]. The bottom electrodes are defined by a lift-off process and consist of a 5-nm-Ti adhesion layer and a 25-nm Pt electrode layer deposited by e-beam evaporation. These are coated with substoichiometric NbO_x layers by reactive sputter deposition of an Nb target using an Ar-O ambient. For comparison, a near-stoichiometric Nb_2O_5 film is also deposited by rf sputtering of an Nb_2O_5 target (Ar ambient). Top electrodes are subsequently defined by a second lift-off process and comprised of 5-nm Nb and 25-nm Pt (or 75 nm Au for the thermoreflectance measurements). A final lithography step is then used to remove the NbO_x film from the contact pads of the bottom electrodes. Details of the deposition conditions and film thicknesses are given in Table I. The resulting cross-point structures have dimensions ranging from $2 \times 2 \mu\text{m}^2$ to $20 \times 20 \mu\text{m}^2$.

The NbO_x stoichiometry is determined by Rutherford backscattering spectrometry (RBS) of films deposited onto vitreous carbon and Si substrates and is found to be in the range from $x = 1.92 (\pm 0.03)$ to $x = 2.6 (\pm 0.05)$. (The relationship between stoichiometry and film resistivity is included in Table I.) Further analysis by grazing incident-angle x-ray diffraction (GIAXRD) shows that the as-deposited films are amorphous. *Ex situ* electrical measurements are performed in air using an Agilent B1500A semiconductor parameter analyzer attached to a Signatone

TABLE I. Film deposition details including the stoichiometry and thickness of each layer.

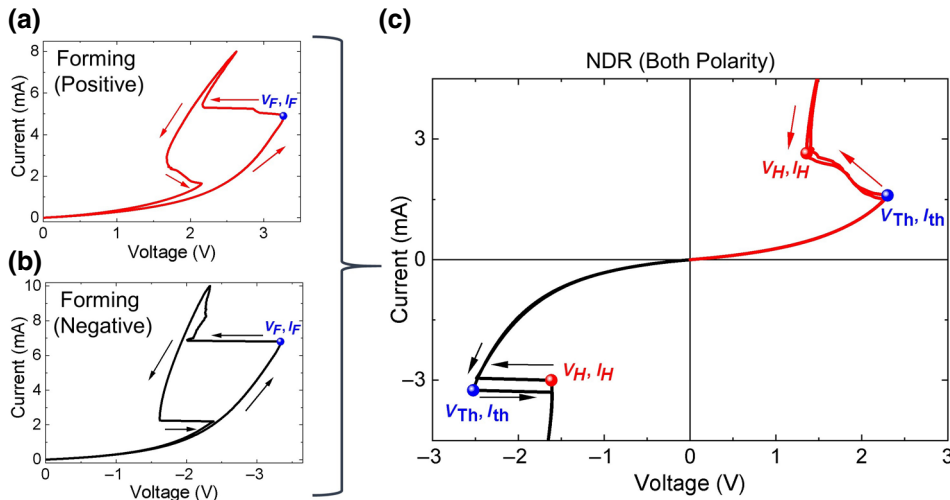
Sputter target	Power (W)	Pressure (mTorr)	Gas flow (Ar/O ₂) sccm/sccm	Thickness (nm)	x in NbO_x	Resistivity ($\Omega \text{ m}$)
Nb_2O_5	180 (rf)	4	20/0	45	2.6 ± 0.05	$3.5 \times 10^4 \pm 1.5 \times 10^3$
Nb	100 (dc)	1.5	19/1	44.3	1.92 ± 0.04	8 ± 1.5
Nb	100 (dc)	2	19/1	55	1.99 ± 0.03	15 ± 1
Nb	100 (dc)	1.5	18.5/1.5	57.3	2.22 ± 0.04	120 ± 7

probe station (S-1160) and generally consist of bidirectional quasistatic current sweeps. *In situ* measurements during thermoreflectance imaging are performed with a Keithley 2410 parameter analyzer and include both dc and pulsed testing. In all cases the bias is applied through the top electrode while the bottom electrode is grounded. Thermal imaging of the devices is performed using the TMX T[°]Imager® system. The imaging setup uses a camera-based thermoreflectance method [33] to infer the temperature rise from the change in surface reflection. The measured map of the temperature rise ΔT is determined by the use of the relation, $\Delta T = (1/C_{TR})(\Delta R/R)$, where ΔR is the change in reflectance of the activated device surface. C_{TR} is the thermoreflectance coefficient of the top electrode material (Au in the present case) obtained from calibration according to $C_{TR} = (1/\Delta T)(\Delta R/R)$, where ΔR is the change in reflectivity of the device surface when subjected to a known temperature rise ΔT .

III. EXPERIMENTAL RESULTS

A. Electroforming and NDR characteristics

All devices with stoichiometric NbO_x films exhibited NDR following a one-off electroforming step but the forming and NDR characteristics are found to depend on the measurement polarity, as illustrated in Fig. 2 for 5-μm NbO_{1.92} devices. During an initial positive bias sweep from 0 → 8 mA [Fig. 2(a)] the device undergoes an electroforming step characterized by a sudden voltage drop at a current around 6 mA and a permanent change in the low-field device resistance from 5 kΩ to 4.5 kΩ (measured at 0.25 V). The impact of electroforming is then clearly evident during the reverse current sweep (from 8 → 0 mA), which shows S-type NDR. Subsequent current sweeps under positive bias continued to show S-type characteristics under both forward and reverse sweeps [similar to that shown by the red line in Fig. 2(c)].



Similar electroforming characteristics are observed under negative bias during the forward sweep from 0 → 10 mA [Fig. 2(b)], with a sudden voltage drop observed at a current of around 7 mA. However, in this case, the reverse current sweep produced a snapback characteristic, with an abrupt voltage increase as the current is reduced to 2.2 mA. Subsequent current sweeps under negative bias show similar snapback characteristics for both forward and reverse sweeps, but at a lower threshold current and voltage [similar to that shown by the black line in Fig. 2(c)]. Once electroformed, devices exhibited characteristics similar to those depicted in Fig. 2(c), regardless of the initial electroforming polarity, i.e., under positive bias they exhibit S-type NDR during forward and reverse current sweeps and under negative bias they exhibited a snapback response.

The permanent changes produced by electroforming are typically attributed to the creation of a filamentary conduction path in the oxide film and/or local breakdown of the Schottky barriers at the metal-oxide interfaces [28]. From a circuit perspective this represents a parallel conduction path within the device and the total device current is divided between the filamentary conduction path and the surrounding device area based on their relative resistances [24]. Indeed, even though the filamentary region may have a higher conductivity, its resistance can exceed that of the surrounding device due to its smaller effective area.

B. *In situ* temperature mapping

In situ thermoreflectance imaging is performed on 10-μm NbO_{1.99} devices to better understand the current distribution during postforming current sweeps. The results are summarized in Fig. 3 and include *in situ* I-V characteristics and the measured temperature distributions for devices subjected to positive and negative bias. Under positive bias the temperature distribution is highly localized in the filamentary region over the entire range of

FIG. 2. Polarity-dependent electroforming and current-controlled NDR characteristics of Pt/Nb/NbO_{1.92}/Pt devices: (a) electroforming of a $5 \times 5 \mu\text{m}^2$ cross-point device under positive bias, (b) electroforming of a different $5 \times 5 \mu\text{m}^2$ cross-point device under negative bias; and (c) typical polarity-dependent switching characteristics of electroformed devices showing a transition from S-type to snapback NDR irrespective of electroforming polarity.

operating currents and the temperature in this region and that of the surrounding film increase monotonically with increasing current. This clearly demonstrates that the resistance of the filamentary path is lower than that of the surrounding device and that the S-type NDR characteristic is dominated by the temperature-dependent conductivity of the filamentary region.

In contrast, under negative bias, the temperature distribution is near uniform at currents below the threshold for snapback and only becomes localized for currents near the threshold value [indicated by the point “F” in Fig. 3(b)]. At this point the temperature increases abruptly while that of the surrounding area decreases, consistent with current redistribution and localization due to the positive feedback created by local Joule heating, as previously reported [28]. This demonstrates that the resistance of the filamentary region is initially comparable to, or greater than that of the surrounding device, but becomes relatively less resistive as the current increases to the threshold value. Such a change implies that the conductivity of the filamentary region increases more rapidly with temperature than that of the surrounding device. For filaments near the center of

the device this may also be facilitated by the nonuniform temperature distribution created by the device geometry [see Fig. 3(c)]. It is important to note that the extent of the filamentary region is smaller than that of the temperature distribution observed at the top electrode surface due to the high thermal conductivity of the metal electrode [25,28].

C. Schottky barriers and polarity-dependent conduction

The temperature-dependent I - V characteristics of an as-fabricated Nb/NbO_{2.22}/Pt device are shown in Fig. 4(a) for both positive and negative bias. Comparison of the device current at equivalent positive and negative voltages clearly highlights the asymmetry in contact resistance created by the Schottky barriers at the metal-oxide interfaces. Similar asymmetry is observed for all NbO_x films used in this study, and is found to increase with increasing device area. From the electron affinity of Nb₂O₅ (3.9 eV) and the work functions of Nb (4.3 eV) and Pt (5.65 eV) the theoretical barrier heights at the Nb-oxide and Pt-oxide interfaces are calculated to be 0.4 and 1.75 eV, respectively [34].

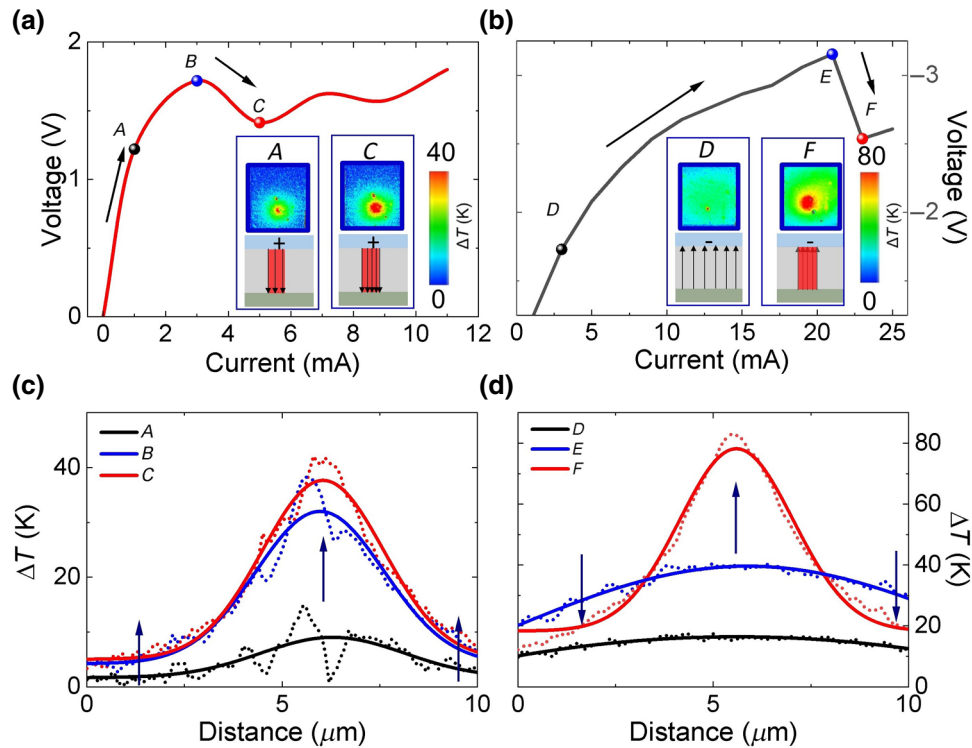


FIG. 3. (a),(b) *In situ* I - V characteristics of a $10 \times 10 \mu\text{m}^2$ Au (75 nm)/Nb(5 nm)/NbO_{1.99}(45 nm)/Pt (25 nm) device showing S-type NDR under positive bias and snapback under negative bias, respectively. Insets show the *in situ* thermoreflectance ($\Delta R/R$) maps of the device for the corresponding bias polarity. (c) Temperature profile through the filamentary region for different current-voltage values during positive bias. (d) Temperature profile of the same device for different current-voltage values during negative bias. The dashed curves in (c) and (d) represent the experimental data and the smooth lines show Gaussian fits of the data. A, B, and C denote subthreshold, threshold, and postthreshold points respectively in the I - V characteristic obtained under positive bias, while D, E, and F denote the same for negative bias polarity.

As a consequence, the contact resistance is expected to be dominated by the Pt-oxide interface, which is under forward bias when negative voltage is applied to the top electrode.

Experimentally, the current-voltage characteristics are analyzed in terms of field-enhanced thermionic emission over a Schottky barrier, as described by [35]

$$I = AA^*T^2e^{-\left(\frac{\Phi_{B0} - \alpha\sqrt{V}}{k_B T}\right)}, \quad (1)$$

where k_B is the Boltzmann constant, T is the absolute temperature, Φ_{B0} is the zero bias potential barrier height at the metal-oxide interface, α is the barrier lowering factor, A^* is the Richardson constant, and A is the device area. For both bias polarities the experimental data for a given electric field (V) exhibits a linear trend on a $\ln(I/T^2)$ vs $1000/T$ plot as shown in Figs. 4(b) and 4(c). The slope of these lines yields an activation energy corresponding to the apparent potential barrier at the particular applied field

(corresponding to V),

$$E = \Phi_{app} = \Phi_{B0} - \alpha\sqrt{V}. \quad (2)$$

The obtained values are found to decrease with increasing applied bias, as expected from Eq. (2) and the zero-bias barrier heights are determined to be 0.19 and 0.24 eV for negative and positive bias, respectively [Fig. 4(d)]. These include contributions from the electrodes and the oxide film and are much lower than the theoretical values. Consequently, they serve as a measure of the resistance asymmetry, rather than actual metal-oxide barrier heights.

The resistance asymmetry is represented more clearly by plotting the ratio of currents measured under negative and positive bias as a function of absolute voltage, as shown for the Nb/NbO_{2.22}/Pt device in Fig. 4(e). This shows that the current ratio (asymmetry) initially increases with increasing voltage before reaching a maximum at 0.75 V and then decreases at higher voltages before saturating at a value between 1 and 2. This behavior is attributed to the dominance of Schottky emission at low fields and an increasing contribution from Poole-Frenkel conduction

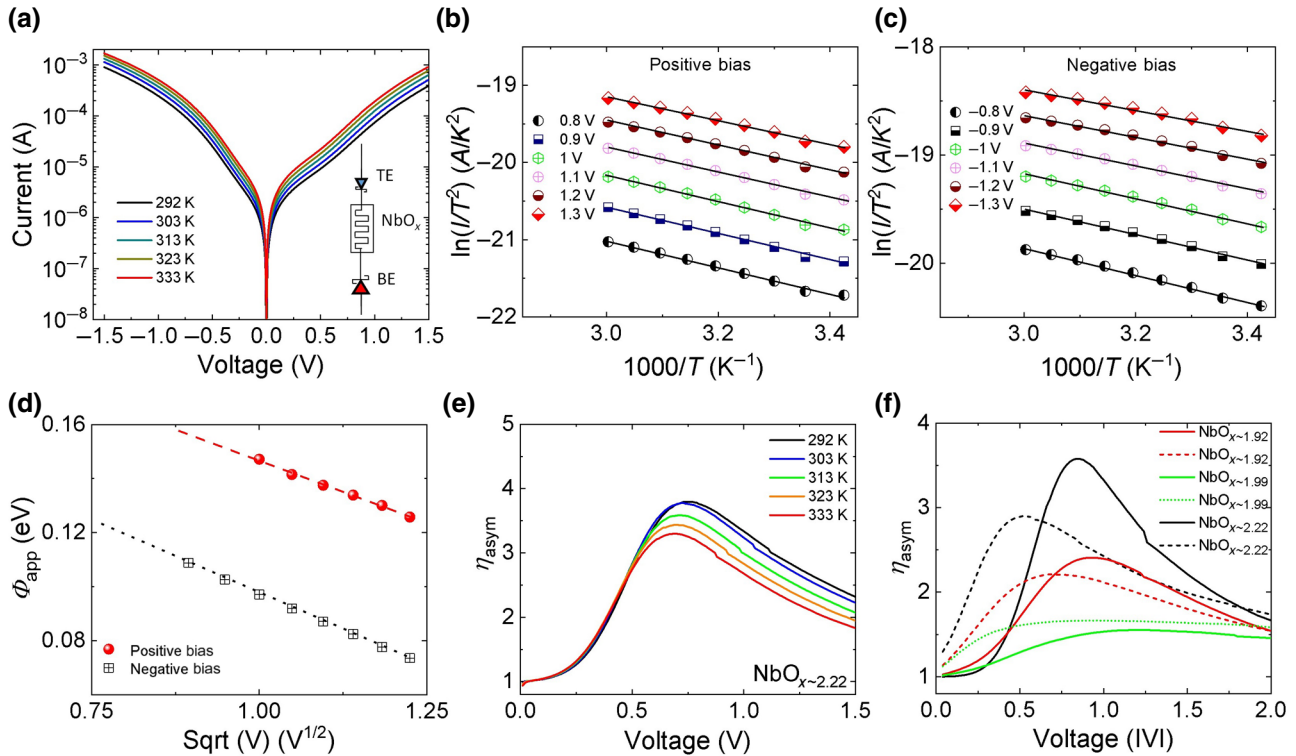
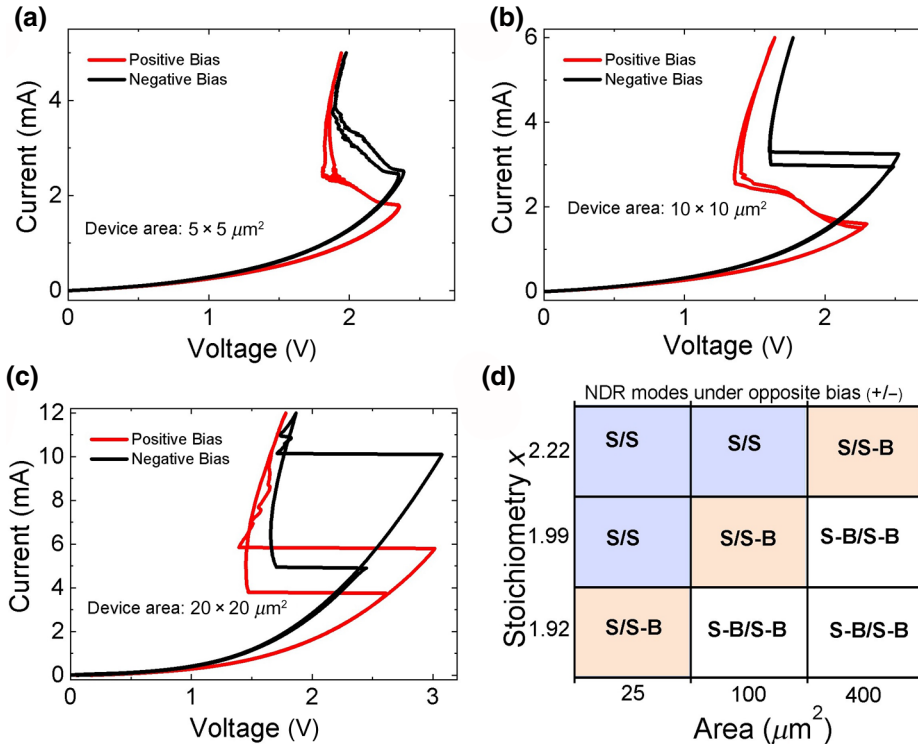


FIG. 4. (a) Temperature-dependent current-voltage characteristics of a typical substoichiometric NbO_x device ($x = 2.22$), with equivalent circuit shown inset, (b),(c) characteristic plots confirming thermionic emission as the major mechanism for Nb top and Pt bottom electrodes ($x = 2.22$), (d) extraction of zero bias potential barrier at the top and bottom interfaces for a typical substoichiometric NbO_x ($x = 2.22$) device, (e) current asymmetry for the data in (a), where η_{asym} is defined as the ratio of device current under negative bias to that under positive bias ($I_{negative}/I_{positive}$), and (f) current asymmetry before and after electroforming for devices with different oxide stoichiometry. Dashed lines in (f) represent the experimental data after electroforming and the smooth lines are the experimental data of the corresponding devices before electroforming.

at higher fields as previously reported for Nb_2O_5 -based Schottky diodes [36]. Significantly, the high-field asymmetry is maintained for all substoichiometric NbO_x films even after electroforming [Fig. 4(f)]. This reflects the fact that the Schottky barriers in the device area surrounding the filamentary region remain unaffected and continue to influence the current distribution in the devices.

D. Effect of oxide stoichiometry and device scaling

The film stoichiometry and device area also have a direct impact on the resistance of the region surrounding the electroformed filament and therefore affect the device characteristics. As a consequence, the behavior reported in Fig. 2 is not universal but is specific to devices with particular combinations of device area and film stoichiometry. A systematic study of these dependencies showed that the smallest area devices ($2 \times 2 \mu\text{m}^2$) displayed smooth S-type NDR under both positive and negative biasing regardless of film stoichiometry. In contrast, larger area devices exhibited one of three behaviors depending on the stoichiometry of the oxide film: dual S-type characteristics [Fig. 5(a)], combined S-type and snapback characteristics [Fig. 5(b)], or dual snapback characteristics [Fig. 5(c)]. These dependencies are summarized in Fig. 5(d), which clearly highlights the three distinct regimes. Note that higher subthreshold and threshold currents are always observed for negative bias polarity, consistent with higher contact resistance from the reverse biased Pt/ NbO_x interface.



IV. DISCUSSION

The above data clearly show that the NDR characteristics of simple two-terminal metal-oxide-metal devices are sensitive to the relative resistances of the filamentary conduction path and the surrounding device area, including effects due to polarity-dependent contact resistance that arise from the metal-oxide contacts. While the dependencies appear complex, they can be understood with reference to a recently developed parallel-memristor or core-shell model of NDR [24].

In its simplest form the core-shell model assumes that the current distribution in postformed MOM structures is localized, with the NDR response dominated by the high current-density filament (core) while the surrounding film (shell) acts as a parallel resistance, as shown schematically in Fig. 6. Analysis then shows that the threshold-switching response depends on the relative magnitudes of the maximum negative differential resistance $|R_{\text{NDR}}|$ of the core and the shell resistances (R_S). Specifically, S-type NDR characteristics are observed when $R_S > |R_{\text{NDR}}|$ and snapback characteristics are observed when $R_S < |R_{\text{NDR}}|$. Since the magnitude of R_S depends on the conductivity (stoichiometry), area (A), and thickness (t) of the oxide film the model predicts a transition from S-type to snapback characteristics for critical values of these parameters, as previously demonstrated [37].

For the case where R_S is independent of bias polarity, the above model predicts either smooth S-type or abrupt snapback characteristics under both positive and

FIG. 5. (a)–(c), Polarity dependent NDRs observed in $\text{Nb}/\text{NbO}_{x \sim 1.99}/\text{Pt}$ MOM cross-point devices with $5 \times 5 \mu\text{m}^2$, $10 \times 10 \mu\text{m}^2$, and $20 \times 20 \mu\text{m}^2$ active area, and (d) matrix representation of dependency of S-type and snapback NDR as a function film stoichiometry, device area, and bias polarity. The notations S/S and SB/SB are used for S-type NDR and snapback NDR, respectively, under subsequent opposite polarity biasing conditions, while S/S-B is used to indicate S-type NDR under positive bias and snapback NDR under negative bias.

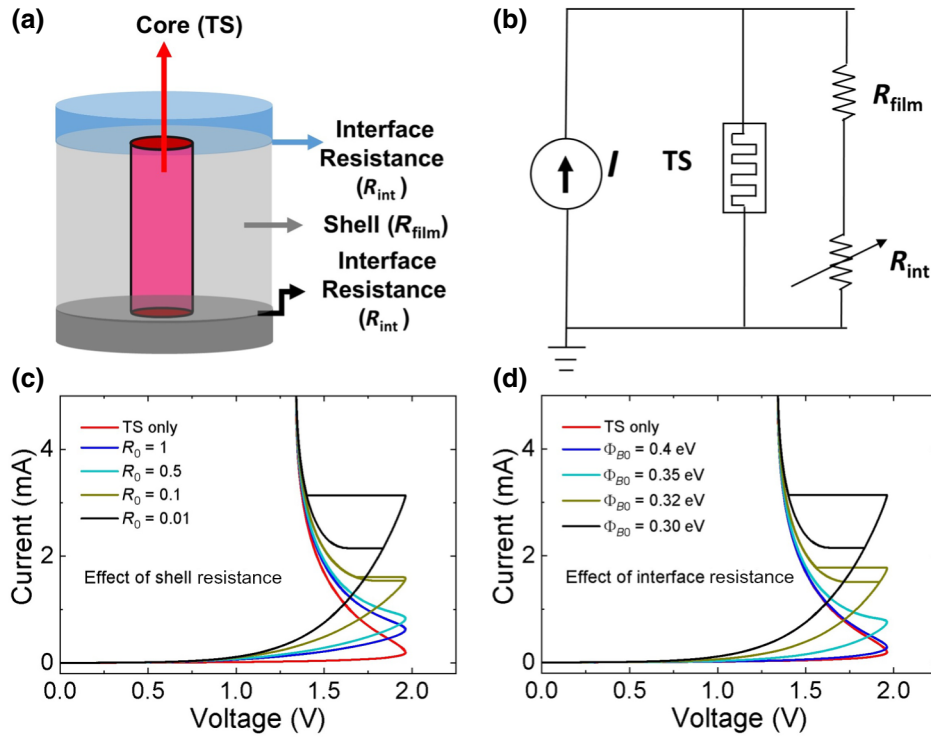


FIG. 6. (a) Schematic of the core-shell model of memristor, (b) circuit model showing a threshold switch (TS) as the core element, a variable resistor indicating the interface resistances at the metal-oxide interfaces and R_{film} represents the oxide resistance in the shell area, which is modeled by the Poole-Frenkel equation, (c) effect of shell resistance on the NDR response, (d) effect of interface resistance (as a function of increasing barrier heights) on the NDR response when the shell resistance (R_{film}) is fixed for a given device area, thickness and oxide stoichiometry. Note that for opposite polarity biasing one interface becomes forward-biased and the other becomes reverse-biased and vice versa, as a result the interface resistance experiences significant change under polarity reversal. Details of the model and the corresponding parameters are given in the Appendix.

negative bias, depending on whether $R_S > |R_{\text{NDR}}|$ or $R_S < |R_{\text{NDR}}|$. However, when R_S is polarity dependent it is necessary to consider three distinct scenarios. Assuming that $R_S = R_p$ under positive bias and $R_S = R_n$ under negative bias and that $R_p > R_n$ we need to specifically consider the three following cases: (i) for $R_p > R_n > R_{\text{NDR}}$, S-type characteristics are expected under both positive and negative bias, as shown in Fig. 5(a); (ii) for $R_{\text{NDR}} > R_p > R_n$, snapback characteristics are expected under both positive and negative bias, as shown in Fig. 5(c); and (iii) for $R_p > R_{\text{NDR}} > R_n$, we expect snapback NDR under negative bias and a smooth S-type NDR under positive bias, as observed in Fig. 5(b). The simple criterion defined by the core-shell model therefore provides the basis for understanding the polarity-dependent switching characteristics and its dependence on film stoichiometry and device area. In this context it is interesting to note that the current asymmetry is almost negligible in stoichiometric Nb_2O_5 as the film resistance in the shell region is much higher than the interface resistance ($R_{\text{film}} > R_{\text{int}}$). As a consequence these devices show symmetric S-type NDR as well as symmetric subthreshold and threshold-switching parameters under

positive and negative bias. This is also evident in the voltage-controlled threshold switching as shown in Fig. 7.

The effect of film stoichiometry and Schottky-barrier heights on NDR characteristics can be illustrated using a lumped-element circuit model implemented in LT-SPICE. In this case, the conductivity of the core and surrounding film are assumed to be governed by Poole-Frenkel conduction with the core temperature determined by Joule heating, and that of the surrounding film assumed to remain at ambient temperature. The shell resistance is additionally assumed to include a contribution from the Schottky barrier created by the metal-oxide interfaces, as governed by the Schottky diode equation [Eq. (1)]. The shell resistance is therefore given by $R_S = R_{\text{film}} + R_{\text{int}}$, as illustrated schematically in Figs. 6(a) and 6(b). Using this model, the I - V characteristics of devices are calculated as a function of film and interface resistance, as shown in Figs. 6(c) and 6(d), respectively. The data clearly demonstrate the transition from smooth S-type to abrupt snapback NDR characteristics as the shell resistance is reduced, and more detailed analysis confirms that this occurs at R_{NDR} . Significantly, a difference in Schottky barrier height of as little as

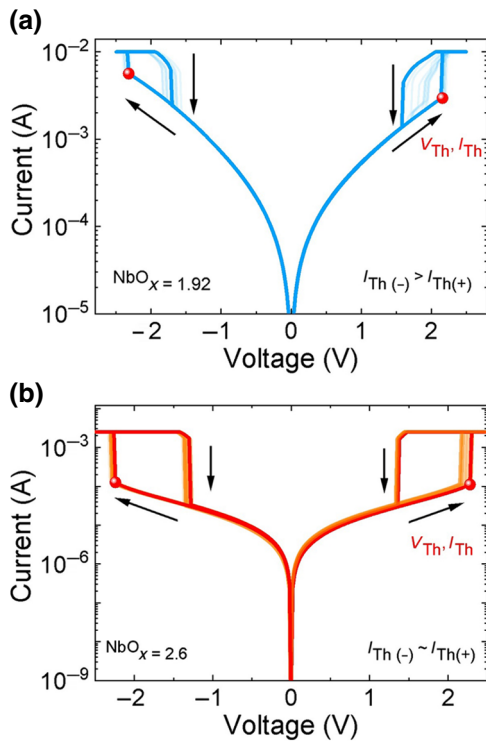


FIG. 7. (a),(b) Asymmetric and symmetric threshold switching in two identical $20 \times 20 \mu\text{m}^2$ devices with substoichiometric NbO_x ($x = 1.92$) and nearly stoichiometric Nb_2O_5 ($x = 2.6$), respectively, under voltage-controlled operation.

0.03 eV is shown to be sufficient to cause such a transition [Fig. 6(d)].

V. CONCLUSION

In summary, we demonstrate polarity-dependent negative differential resistance characteristics in $\text{Nb}/\text{NbO}_x/\text{Pt}$ cross-point devices and show that the observed asymmetry is a direct consequence of the Schottky barriers

created by the metal-oxide contacts. Three distinct behaviors are observed under opposite polarity testing: bipolar S-type NDR, bipolar snap-back NDR, and combined S-type and snapback NDR, depending on the stoichiometry of the oxide film and device area. By combining *ex situ* current-controlled electrical measurements and *in situ* thermoreflectance imaging we show that these NDR responses are associated with strong current localization within the device. This is used to justify the use of a previously developed two-zone, core-shell thermal model of the device. The observed polarity-dependent NDR responses, and their dependence on stoichiometry and area are then explained by extending this model to include the effect of the polarity-dependent contact resistance. Our extended model provides improved understanding of the NDR response of metal-oxide-metal structures and informs the engineering of devices for neuromorphic computing and nonvolatile memory applications.

ACKNOWLEDGMENTS

This work is partly funded by an Australian Research Council (ARC) Linkage Project (LP150100693) and Varian Semiconductor Equipment/Applied Materials. We also acknowledge the Australian Facility for Advanced ion-implantation Research (AFAiiR), a node of the NCRIS Heavy Ion Accelerator Capability, and the Australian National Fabrication Facility (ANFF) ACT node for access to their research facilities and expertise.

There are no conflicts of interest to declare.

APPENDIX: SPICE MODELS

Device characteristics are simulated using an LT-SPICE model of the circuit shown in Fig. 6(b), where the interface resistance is represented by a Schottky contact [Eq. (1)], and the core and shell resistances are attributed to Poole-Frenkel conduction, and represented by equations of the

TABLE II. Memristor parameters used in simulation for core memristor and shell resistance in the Poole-Frenkel model.

Model parameters (unit)	Symbol	Threshold switch (core)	Shell resistance, R_{film}	Schottky parameters
Thermal capacitance (J K^{-1})	C_{th}	1×10^{-15}		
Resistance prefactor (Ω)	R_0	80	0.01 to 1	
Thermal resistance (K W^{-1})	R_{th}	2×10^5	2×10^5	
Ambient temperature (K)	T_{amb}	298	298	
Activation energy (eV)	E_a	0.23	0.23	
Relative permittivity of the threshold-switching volume and surrounding NbO_x film	ϵ_r	45	45	
Richardson's constant ($\text{A K}^{-2} \text{ m}^{-2}$)	A^*			480
Barrier lowering factor $\text{eV}^{1/2}$	α			0.24
Zero bias barrier height (eV)	Φ_{B0}			0.3 to 1
Schottky diode area (m^2)	A			2.48×10^{-11}
Film thickness (nm)		45		

form [6]

$$R_m = R_0 e^{\frac{1}{k_B T} \left(E_a - q \sqrt{\frac{qE}{\pi \epsilon_0 \epsilon_r}} \right)}, \quad (\text{A1})$$

where k_B is the Boltzmann constant, E_a is the activation energy, ϵ_0 is the vacuum permittivity, and ϵ_r is the relative permittivity of the threshold-switching volume and surrounding NbO_x film. R_0 is resistance prefactor.

The dynamic behavior of the memristor is then defined by Newton's law of cooling:

$$\frac{dT_m}{dt} = \frac{I_m^2 R_m}{C_{\text{th}}} - \frac{\Delta T}{R_{\text{th}} C_{\text{th}}}, \quad (\text{A2})$$

where R_{th} and C_{th} are the thermal resistance and the thermal capacitance of the device, and ΔT is change in temperature due to Joule heating.

Details of the model parameters are given in Table II.

- [1] X. Liu, S. Li, S. K. Nandi, D. K. Venkatachalam, and R. G. Elliman, Threshold switching and electrical self-oscillation in niobium oxide films, *J. Appl. Phys.* **120**, 124102 (2016).
- [2] S. Li, X. Liu, S. K. Nandi, D. K. Venkatachalam, and R. G. Elliman, Coupling dynamics of $\text{Nb}/\text{Nb}_2\text{O}_5$ relaxation oscillators, *Nanotechnology* **28**, 125201 (2017).
- [3] S. K. Nandi, S. Li, X. Liu, and R. G. Elliman, Temperature dependent frequency tuning of NbO_x relaxation oscillators, *Appl. Phys. Lett.* **111**, 202901 (2017).
- [4] S. Li, X. Liu, S. K. Nandi, D. K. Venkatachalam, and R. G. Elliman, High-endurance megahertz electrical self-oscillation in Ti/NbO_x bilayer structures, *Appl. Phys. Lett.* **106**, 212902 (2015).
- [5] S. Kumar, Z. Wang, N. Davila, N. Kumari, K. J. Norris, X. Huang, J. P. Strachan, D. Vine, A. D. Kilcoyne, Y. Nishi, and R. S. Williams, Physical origins of current and temperature controlled negative differential resistances in NbO_2 , *Nat. Commun.* **8**, 658 (2017).
- [6] S. Slesazeck, H. Mähne, H. Wylezich, A. Wachowiak, J. Radhakrishnan, A. Ascoli, R. Tetzlaff, and T. Mikolajick, Physical model of threshold switching in NbO_2 based memristors, *RSC Adv.* **5**, 102318 (2015).
- [7] J. M. Goodwill, G. Ramer, D. Li, B. D. Hoskins, G. Pavlidis, J. J. McClelland, A. Centrone, J. A. Bain, and M. Skowronski, Spontaneous current constriction in threshold switching devices, *Nat. Commun.* **10**, 1628 (2019).
- [8] J. M. Goodwill, D. K. Gala, J. A. Bain, and M. Skowronski, Switching dynamics of TaO_x -based threshold switching devices, *J. Appl. Phys.* **123**, 115105 (2018).
- [9] A. A. Sharma, M. Noman, M. Abdelmoula, M. Skowronski, and J. A. Bain, Electronic instabilities leading to electroformation of binary metal oxide-based resistive switches, *Adv. Funct. Mater.* **24**, 5522 (2014).
- [10] A. Mansingh and R. Singh, The mechanism of electrical threshold switching in VO_2 crystals, *J. Phys. C: Solid State Phys.* **13**, 5725 (1980).
- [11] D. Li, A. A. Sharma, N. Shukla, H. Paik, J. M. Goodwill, S. Datta, D. G. Schlom, J. A. Bain, and M. Skowronski, ON-state evolution in lateral and vertical VO_2 threshold switching devices, *Nanotechnology* **28**, 405201 (2017).
- [12] A. Alexandrov, A. Bratkovsky, B. Bridle, S. Savel'Ev, D. Strukov, and R. S. Williams, Current-controlled negative differential resistance due to Joule heating in TiO_2 , *Appl. Phys. Lett.* **99**, 202104 (2011).
- [13] M. J. Lee, S. E. Ahn, C. B. Lee, C. J. Kim, S. Jeon, U. I. Chung, I. K. Yoo, G. S. Park, S. Han, and I. R. Hwang, A simple device unit consisting of all NiO storage and switch elements for multilevel terabit nonvolatile random access memory, *ACS Appl. Mater. Interfaces* **3**, 4475 (2011).
- [14] S. Kumar, J. P. Strachan, and R. S. Williams, Chaotic dynamics in nanoscale NbO_2 Mott memristors for analogue computing, *Nature* **548**, 318 (2017).
- [15] J. Lappalainen, J. Mizsei, and M. Huotari, Neuromorphic thermal-electric circuits based on phase-change VO_2 thin-film memristor elements, *J. Appl. Phys.* **125**, 044501 (2019).
- [16] M. D. Pickett and R. S. Williams, Phase transitions enable computational universality in neuristor-based cellular automata, *Nanotechnology* **24**, 384002 (2013).
- [17] S. Yu, Neuro-inspired computing with emerging non-volatile memories, *Proced. IEEE* **106**, 260 (2018).
- [18] L. Chua, V. Sbitnev, and H. Kim, Neurons are poised near the edge of chaos, *Int. J. Bifurcat. Chaos* **22**, 1250098 (2012).
- [19] L. Chua, Memristor, Hodgkin–Huxley, and edge of chaos, *Nanotechnology* **24**, 383001 (2013).
- [20] W. Yi, K. K. Tsang, S. K. Lam, X. Bai, J. A. Crowell, and E. A. Flores, Biological plausibility and stochasticity in scalable VO_2 active memristor neurons, *Nat. Commun.* **9**, 4661 (2018).
- [21] M. D. Pickett, G. Medeiros-Ribeiro, and R. S. Williams, A scalable neuristor built with Mott memristors, *Nat. Mater.* **12**, 114 (2013).
- [22] S. K. Nandi, X. Liu, D. K. Venkatachalam, and R. G. Elliman, Threshold current reduction for the metal–insulator transition in NbO_{2-x} selector devices: The effect of ReRAM integration, *J. Phy. D: Appl. Phys.* **48**, 195105 (2015).
- [23] A. Beaumont, J. Leroy, J. C. Orlanges, and A. Crunteanu, Current-induced electrical self-oscillations across out-of-plane threshold switches based on VO_2 layers integrated in crossbars geometry, *J. Appl. Phys.* **115**, 154502 (2014).
- [24] S. Li, X. Liu, S. K. Nandi, S. K. Nath, and R. G. Elliman, Origin of current-controlled negative differential resistance modes and the emergence of composite characteristics with high complexity, *Adv. Funct. Mater.* **29**, 1905060 (2019).
- [25] S. K. Nath, S. K. Nandi, S. Li, and R. G. Elliman, Detection and spatial mapping of conductive filaments in metal/oxide/metal cross-point devices using a thin photoresist layer, *Appl. Phys. Lett.* **114**, 062901 (2019).
- [26] S. Li, X. Liu, S. K. Nandi, and R. G. Elliman, Anatomy of filamentary threshold switching in amorphous niobium oxide, *Nanotechnology* **29**, 375705 (2018).

- [27] S. K. Nath, S. K. Nandi, S. Li, and R. G. Elliman, Metal–oxide interface reactions and their effect on integrated resistive/threshold switching in NbO_x , *Nanotechnology* **31**, 235701 (2020).
- [28] S. K. Nandi, S. K. Nath, A. El-Helou, S. Li, T. Ratcliff, M. Uenuma, P. E. Raad, and R. G. Elliman, Electric field and current induced electroforming modes in NbO_x , *ACS Appl. Mater. Interfaces* **12**, 8422 (2020).
- [29] G. A. Gibson, S. Musunuru, J. Zhang, K. Vandenberghe, J. Lee, C. C. Hsieh, W. Jackson, Y. Jeon, D. Henze, Z. Li, and R. S. Williams, An accurate locally active memristor model for S-type negative differential resistance in NbO_x , *Appl. Phys. Lett.* **108**, 023505 (2016).
- [30] G. A. Gibson, Designing negative differential resistance devices based on self-heating, *Adv. Funct. Mater.* **28**, 1704175 (2018).
- [31] T. Mikolajick, H. Wylezich, H. Maehne, and S. Slesazeck, Versatile resistive switching in niobium oxide, *IEEE International Symposium on Circuits and Systems (ISCAS*, 2016), p. 381.
- [32] D. Y. Cho, M. Luebben, S. Wiefels, K. S. Lee, and I. Valov, Interfacial metal–oxide interactions in resistive switching memories, *ACS Appl. Mater. Interfaces* **9**, 19287 (2017).
- [33] A. El Helou, P. E. Raad, A. Venugopal, and D. Kande, in ASME 2018 International Technical Conference and Exhibition on Packaging and Integration of Electronic and Photonic Microsystems, (American Society of Mechanical Engineers, 2018), pp. V001T003A002–V001T003A002.
- [34] P. Periasamy, H. L. Guthrey, A. I. Abdulagatov, P. F. Ndione, J. J. Berry, D. S. Ginley, S. M. George, P. A. Parilla, and R. P. O’Hayre, Metal–insulator–metal diodes: Role of the insulator layer on the rectification performance, *Adv. Mater.* **25**, 1301 (2013).
- [35] L. Michalas, M. Trapatseli, S. Stathopoulos, S. Cortese, A. Khiat, and T. Prodromakis, Interface asymmetry induced by symmetric electrodes on metal–Al: TiO_x –metal structures, *IEEE Trans. Nanotech.* **17**, 867 (2017).
- [36] N. Alimardani, J. M. McGlone, J. F. Wager, and J. F. Conley, Jr., Conduction processes in metal–insulator–metal diodes with Ta_2O_5 and Nb_2O_5 insulators deposited by atomic layer deposition, *J. Vac. Sci. Technol., A* **32**, 01A122 (2014).
- [37] S. K. Nandi, S. K. Nath, A. E. Helou, S. Li, X. Liu, P. E. Raad, and R. G. Elliman, Current localisation and redistribution as the basis of discontinuous current controlled negative differential resistance in NbO_x , *Adv. Funct. Mater.* **29**, 1906731 (2019).